Importance of outliers: a three dimensional study of coarsening in α phase iron

Yu-Feng Shen,[1] S. Maddali,[1] D. Menasche,[1] A. Bhattacharya,[2] G.S. Rohrer,[2] and R. M. Suter[1, *]

[1]*Department of Physics, Carnegie Mellon University, Pittsburgh, PA 15213*
[2]*Department of Materials Science and Engineering,*
Carnegie Mellon University, Pittsburgh, PA 15213
(Dated: June 10, 2019)

Grain coarsening behavior in an alpha phase iron sample is studied in three dimensions using high energy x-ray diffraction microscopy. 4,971 grains that are entirely inside the sample are segmented in the initial state and 3,905 remain after annealing. A matching procedure was used to track 3,299 grains between the two states while the remainder were either consumed by neighbors or the tracking algorithm failed to correlate them. During the single annealing treatment, the average grain volume increased by 13%. Statistical analysis in each state yields subtle changes in the grain size and nearest neighbor number distributions. Correlating topological features with volume changes between states, the average behavior is seen to be consistent with an isotropic model of curvature driven coarsening, but the dispersion of volume changes in each topological class is comparable to the overall trend in the average behaviors. Thus, the topological characterizations used here are not predictive of the behavior of individual grains under the isotropic assumption. Examination of anecdotal cases allows understanding of some outliers but others appear counter to an isotropic theory.

I. INTRODUCTION

Many condensed matter systems undergo coarsening processes in which the average cell size in a large ensemble increases over time as large cells intrude on and consume smaller cells. This process is typically driven by reduction in the total interfacial energy, and, thus the total interfacial area. Examples are as diverse as foams, [1–3] phase separating liquids and solids, and polycrystalline aggregates. [4–6] For fluid systems, all interfaces have the same structure and properties, so the driving forces for motion can be modeled with a single homogeneous interfacial tension and mobility. Curved boundaries are expected to move toward their centers of curvature since this results in reduced local boundary areas. This flattening of boundaries tends to lead to polyhedral domain shapes.

For the case of coarsening in polycrystalline microstructures, the homogeneity condition is broken due to anisotropic crystal properties which result in the energies and mobilities of crystal-crystal interfaces being dependent on both the relative crystal orientations and the local orientation of the interface normal. Thus, boundaries between crystals or grain boundaries are characterized on the mesoscale by five parameters: for example, three disorientation parameters defining the symmetry reduced relative orientations of crystal unit cells and two parameters that define the local interface normal relative to unit cells of the two crystals. These (or alternative) sets of five degrees of freedom define the "grain boundary character" (GBC) [7] and coarsening is expected to depend on the distribution (GBCD) and connectivity of the boundary types. Finally, it should be noted that the interface motions described here are expected to dominate

microstructure and boundary evolution only after bulk (grain interior) defect densities and their associated bulk excess energies have been reduced to negligible values. However, local irreducible strain fields associated with grain boundaries may well influence boundary energies and mobilities.

Because microstructure plays a key role in determining the properties [8–10] of polycrystalline materials that are used throughout modern societies, coarsening or "grain growth," has been studied experimentally and theoretically for many decades. [11–14] For two dimensional systems, the basis for most theoretical and experimental investigations[15, 16] is the von Neumann-Mullins "$n - 6$ rule"[5, 6],

$$\frac{dA}{dt} = \frac{\pi}{3} M \gamma (n - 6), \qquad (1)$$

where $\frac{dA}{dt}$ is the rate of area change of the "two dimensional grain", n is the number of grain sides, M is the mobility and γ is the excess energy per unit length of boundary. This predicts that cells with more than six sides (or neighbors) will grow while those with fewer than six sides will shrink and eventually disappear. The simple form of (1) results from the assumption of homogeneity of boundary properties (hence the single values of M and γ) and it assumes mechanical equilibrium at vertices which implies triple point vertex angles of 120°.

Palmer et al. [17] compared (1) with experimental observations of thin organic polycrystalline films and found significant deviations from the expected vertex angles but nevertheless found that the trend in average growth rates in each topological class agreed well; however, large deviations, of the same order as the overall trend, were observed within each class. One suggested cause of deviations from $n - 6$ was the heterogeneity in boundary properties. Since the optical measurement did not determine crystal orientations, it was not possible to classify

* Corresponding author: suter@andrew.cmu.edu

the boundaries.

More than 50 years after von Neuman's and Mullins' work, a rigorous three dimensional (3D) generalization of (1) has been obtained by McPherson and Srolovitz, [4] the "M-S relation,"

$$\frac{dV}{dt} = \frac{\pi}{3} M\gamma \left(\mathcal{M} - 6\mathcal{L}_{grain} \right), \qquad (2)$$

where $\frac{dV}{dt}$ is the rate of grain volume change, M is the mobility, γ is the excess energy per unit area of boundary, $\mathcal{M}$ is the total triple line length around the grain and $\mathcal{L}_{grain}$ is the mean width of the grain. [4] Again, this result is based on homogeneous, isotropic grain boundary properties and therefore on the expectation of uniform 120° dihedral angles at triple lines where three grains meet.

It is only within the past decade that experiments have begun to be able to watch internal three dimensional microstructures evolve over time. The key development has been the application of diffraction methods using high flux, tunable synchrotron x-rays. Spatially resolved diffraction techniques have been developed that are able to image microstructures in three dimensions including crystalline grain unit cell orientations, grain shapes and positions; the non-destructive measurements allow collection of images of volumes of interest in successive states of evolution. [18–22] These measurements yield novel data sets spanning large ensembles of grains and grain boundaries. Extraction of either statistical characteristics of grains or local characteristics such as individual boundary motions requires development of trusted computational tools and careful consideration of measurement resolution in both position and orientation degrees of freedom.

Two distinct data collection methods have been used in the above studies. Zhang et al. [23], and McKenna et al. [24] apply diffraction contrast tomography (DCT) [21] using data collected at the European Synchrotron Radiation Facility. Sun et al. [25] use a commercial, laboratory based DCT system. [26] Work at the Advanced Photon Source has applied near-field high energy diffraction microscopy (nf-HEDM) [19, 27, 28] which is an implementation of 3DXRD. [20] While nf-HEDM uses a line focused beam to illuminate a series of quasi-two dimensional cross-sections which are then stacked to yield three dimensional grain geometries, DCT uses a "box" beam to illuminate a volume of microstructure. Reconstruction approaches are quite different [21, 29] but, for the well ordered grain structures of interest to coarsening, results have comparable resolutions of grain orientations and grain boundary positions.

Recent observations of coarsening using the above diffraction based methods include studies of iron, [23, 25, 30] nickel, [31, 32] and strontium titanate. [33] Similar work was carried out using absorption tomography combined with grain boundary segregation in a titanium alloy. [24] Real time growth of individual selected grains based on evolution of a single spatially resolved Bragg peak have also been recorded. [34] Direct comparisons to computational phase field or finite element models have been carried out in a small number of cases. [24, 33]

Here, we present statistical analysis of data, also studying alpha iron, first presented in the thesis of S. Maddali. [30] This data set comprises a larger statistical sampling of grains in than previous work, by roughly a factor of 10, and therefore yields improved statistical distributions, but only two time steps are measured compared to 15 in Zhang *et al.* [23]. Further work addressing boundary motions and making comparisons to computational models of evolution can be expected to follow in all of these cases.

II. METHODOLOGY

A. Sample preparation and data collection

The sample material was electrolytically grown high-purity iron (obtained from the Center for Iron and Steel-making Research at Carnegie Mellon University) and with an elongated grain structure. At temperatures below 912 C, iron exists in its [-allotropic] alpha phase form, which has a body-centered cubic (BCC) crystal structure. The requirement of (statistically) isotropic grain boundary inclinations required the destruction of the elongated grain structure followed by regrowth through annealing and quenching. Accordingly, the sample was rolled in a mill from an original thickness of about 5 mm to about 1 mm and annealed in a tube furnace for two hours at 600 C in a forming gas atmosphere ($N_2 + 3\%H_2$) and then quenched. A sample of approximate dimensions $1 \times 1 \times 30$ mm^3 was cut from this material.

Measurements were performed using the nf-HEDM apparatus in the E-hutch of beamline 1-ID at the Advanced Photon Source at Argonne National Laboratory. [19, 28] A 65.351 keV x-ray beam was focused vertically to a ≈ 1.5 μm full width at half maximum line beam. The beam size was limited in the horizontal direction to 1.5 mm using slits. As the sample was continuously rotated about a vertical axis perpendicular to the beam plane, images of diffraction spots were collected over successive angular intervals of width $\delta\omega = 0.25°$. The total rotation range was 180° over which typical orientations generate roughly ≈ 180 observed Bragg peaks. The high resolution imaging detector used a scintillator (LuAG) whose scintillation light was optically coupled to a 2k $\times$ 2k CCD camera; using a 5X objective lens, the effective pixel size was 1.54 μm. This rotation procedure was repeated at two different sample-to-detector distances and the data collection was repeated for multiple equally-spaced sample layers by translating the sample perpendicular to the beam; in this manner diffraction data from an entire volume was collected. Here, 65 layers with $3\mu m$ spacing were measured, so a total volume of about 1 mm $\times$ 1mm $\times$ 0.195 mm^3 was measured. After the first volume measurement, the sample was removed

from its mount and annealed in a tube furnace at 600 C for half an hour again using a forming gas atmosphere. The sample was replaced in the HEDM apparatus and the same volume of the sample was measured again. For further details of the sample and procedure, the reader is referred to the Ph.D. thesis of Maddali [30].

B. nf-HEDM reconstruction, volume registration and grain segmentation

The reconstruction of sample microstructure is performed with the forward modeling software *IceNine* [19, 29] after image analysis that separates diffraction signals from background. [35] A critical feature of the image analysis is the use of a Lapacian-of-Gaussian edge detection algorithm that has been shown to yield diffraction spot shapes reflective of projected images of each diffracting grain cross-section. [36] For each measured layer, the reconstruction was performed on a simulation space which is larger than the illuminated sample cross-section. A mesh of $s = 1.56$ μm side-length equilateral triangles spanned the simulation space; each triangle encloses an area corresponding to a square with side length 0.581 μm. In each layer, there are about 10^6 triangular voxels. For each triangular element, the assigned orientation is that which generates the maximum overlap between simulated and experimental diffraction spots. For mesh elements near grain boundaries, even at the optimal orientation, the simulation will miss some diffraction spot edges due to detector discretization and image analysis noise; this leads to a decreased confidence or overlap metric. [19] Similarly, diffraction signals from two (or more) neighboring grains' orientations can each generate finite overlap of simulated diffraction. The optimization algorithm simply picks the orientation with maximal overlap for each mesh element. The large number of Bragg peak observations has the effect of signal averaging over the various noise sources and leads to ~ 1 μm accuracy in relative grain boundary positions within the reconstruction planes. [36]

The open source software package, *DREAM.3D*, [37] was used to segment the reconstructed data into individual grains. Before using *DREAM.3D*, the data were down-sampled from the set of reconstructed layer-by-layer *.mic* files to a single *.h5ebsd* file, with $3 \times 3 \times 3$ μm^3 cubic voxels; orientations were assigned as that of the nearest voxel in the *.mic* files. The orientation of each voxel is compared to its neighbors (in 3D) and contiguous sets of voxels with orientations that differ by $\leq 2°$ were grouped together as grains; the minimum size of accepted grains was set to eight voxels. Those groups with fewer than eight voxels (i.e., < 216 μm^3 or < 7.4 μm spherical equivalent diameter) were treated as gaps in the microstructure. Less than 0.1% of voxels were in such gaps; gaps were then eliminated by dilating neighboring grains uniformly using a procedure in *DREAM.3D*. The aggressive down sampling described here yields a hard

TABLE I: Numbers and dimensions of grains in two sample states.

State	Total	Internal	Internal Grains		
			$V_T(10^7\mu\text{m}^3)$	$\langle V \rangle(10^4\mu\text{m}^3)$	$D_{eff}(\mu\text{m})$
0	10,927	4,971	5.96	1.20	28.4
1	9,224	3,905	5.28	1.35	29.6

lower cutoff in the grain size distribution at a level above the expected minimum size to which the measurement is sensitive.

The analysis below is restricted to grains that are entirely inside the measured volume in both states. First, any grain whose centroid lies outside the black boundary in Fig. 1 is removed to avoid surface effects. Further, any grain that intersects the top or bottom edge of the reconstructed volume is also excluded from analysis. This method is similar to that used in Rowenhorst *et al.* [38] to avoid statistical bias from cut-off grains; however, as discussed below, the procedure also preferentially eliminates large grains. Global statistics are shown in Table I. V_T is the total volume occupied by internal grains, $\langle V \rangle$ is the average grain volume, and $D_{eff} = 2 \left(\frac{3}{4\pi} \langle V \rangle \right)^{1/3}$, is the average spherical equivalent diameter (SED). Note that D_{eff} is the SED of a grain with the average volume, not the average of SED values. The nominal trimmed measured sample volume is $\approx 1.3 \times 10^8 \mu\text{m}^3$ in both states.

Because it is not possible to re-mount the sample in exactly the same position and orientation after annealing, volume registration was required in order to correlate local properties before and after annealing. Registration was done in two steps [30]:

1. Determine the single rigid-body translation and rotation that aligns a single layer in the post-anneal volume with its corresponding layer in the pre-anneal volume, and apply this transformation to all layers in the post-anneal volume. This transformation was determined "by eye."

2. Pick one grain that is present in both volumes and rotationally align the entire post-anneal volume such that the two orientations of this grain coincide.

After this process, the angular alignment of the two volumes is within $\approx 0.1°$ which is the expected experimental resolution. Fig. 1 shows the final 3-D registered reconstructions of the α-iron sample before and after annealing.

C. Grain matching

To study coarsening dynamics, it is necessary to identify the same grain in different time step snapshots. For
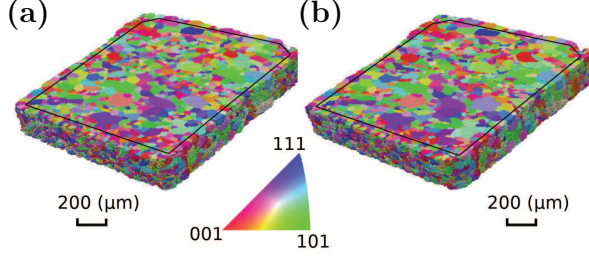
FIG. 1. The measured sample volume, (a) before and (b) after annealing. Black lines indicate schematically a trimming of the sample edges used to avoid the damaged surface region that has anomalously small grains. Colors are according to the inverse pole figure key shown and is referenced to the normal direction to the square cross-section.

each grain in one state, we search every grain within a surrounding volume of the other state and, if both the misorientation angle and volume ratio are within specified thresholds we call the pair a match. A detailed description is provided in Algorithm 1.

Algorithm 1 Grain matching

Parameters: *MisorLim, VolRatLim, DistDiaLim*

1: **procedure** GRAIN MATCHING
2:     **for** *grain A_i* **in** State 0 **do**
3:         $D_A \leftarrow$ Diameter of A_i
4:         $S_A \leftarrow$ Centroid of A_i
5:         $V_A \leftarrow$ Volume of A_i
6:         **for** *grain B_j* **in** State 1 **do**
7:             $S_B \leftarrow$ Centroid of B_j
8:             **if** $|S_A - S_B| \leq DistDiaLim \times D_A$ **then**
9:                 $V_B \leftarrow$ Volume of B_j
10:                **if** $\frac{1}{VolRatLim} \leq V_A/V_B$
                              $\leq VolRatLim$ **then**
11:                   **if** Misorientation of A_i and $B_j \leq$
                           MisorLim **then**
12:                     Match B_j to A_i

To ensure robustness, grain matching is performed in both directions; that is, for each grain in the initial state, we search for the same grain in the final state and for each grain in the final state we search for the same grain in the the initial state. Only matched pairs that are the same in both directions are kept for further analysis. The values $0.5°, 10, 2$ were chosen as *MisorienLim, VolRatioLim, DistToDiaLim*, respectively. These relatively strict limits result in 3299 pairs of matched grains. 30.2% of grains in the initial state are not matched in the annealed state whereas only 12.4% of final state grains are not located in the initial state. This disparity is largely attributed to small grains being consumed by larger ones and thus not existing in the annealed state. Assuming that new grains are not nucleated, the 12.4% missing in the reverse matching must be characteristic of the difficulty in matching small grains (many of which exist in both states since some grains

are always shrinking and disappearing). Further characterization of matched and unmatched grains is given in Appendix B.

Fig. 2 shows some examples of matched grain pairs. It is seen qualitatively that, in most cases, grain boundaries move toward their centers of curvature as expected for capillarity driven growth.
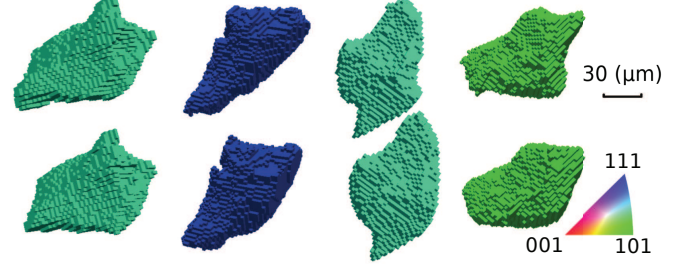

FIG. 2. Examples of matched grains, top row before annealing and bottom row after annealing. The roughness of the surfaces is due to the discrete voxel size; no smoothing has been performed. The side length of each cubic voxel is $3~\mu$m. Colors correspond to the crystal unit cell orientations according to the inverse pole figure scheme illustrated at bottom right.

III. RESULTS

A variety of data sets characterizing three dimensional statistics of grains in specific states or "snapshots" are in the literature, for example, see [23, 38]. Non-destructive measurements allow comparisons of such statistics in multiple snapshots of the same material volume. The next section presents analyses that do not require tracking of individual grains but which do require the restriction to grains that are entirely enclosed within the sample and the measured volumes. The following section presents statistical analyses of the evolution of individual grains.

A. Statistical distributions of grain characteristics

a. Grain size distributions. The number of internal grains decreased from 4971 to 3905 with annealing; as listed in Table I this corresponds to an average grain volume increase from $\approx 11,993~\mu$m^3 to $\approx 13,533~\mu$m^3 or a $\approx 13\%$ volume increase or a 4% increase in linear dimension.

Individual grain volumes are extracted from the data sets as $V_g = V_{vox}N_g = (27~\mu\text{m}^3)~N_g$, the volume per voxel (see Sec. II B) times the number of voxels assigned to the grain. As shown in Fig. 3a, the measured grain volumes in each state span more than three decades even with the lower end cutoff at $N_g = 2^3 = 8$ contiguous voxels. Similarly, the large number of grains in the data set allows the probability density to be resolved over at least four

decades. The observed distribution of volumes is monotonically decreasing. A more conventional "size distribution" in terms of spherical equivalent radii is shown in Fig. 3b; not surprisingly, this distribution extends over about one order of magnitude as seen in numerous other data sets. [23, 24, 38] The conservative small size cutoff used in this analysis results in the plot terminating just below the peak value. Error bars in both plots are derived from Poisson counting statistics related to the number of entries in each displayed bin. We next discuss the interpretation of the distributions and the relation between them.

Since the grain volume is a continuous variable, an appropriate way to characterize the distribution is with a probability density function, $P(V)$, where $P(V)dV$ is the probability of a grain having size V within the interval dV. In a large ensemble of N grains, the number within dV is $dN = NP(V)dV$. The goal is to approximate the distribution, $P_\infty(V)$, that would be observed in a very large (or infinite) ensemble. Fig. 3a plots empirical approximations to this distribution function for each of the measured states: $P_N(V) \approx \frac{\Delta N}{N} \frac{1}{\Delta V}$ with ΔN being the number of grains within ΔV of the nominal volume and N the total number of grains in each state. In Fig. 3a, bin widths are chosen such that $\frac{\Delta V}{V} \approx 0.26$ (more precisely, $\frac{V+\Delta V}{V} = 10^{0.1}$) which assures that the apparent $P_N(V)$ is roughly linear over each bin interval and the differential approximation is reasonable. $P_N(V)$ is seen to be monotonically decreasing and changes only slightly during the observed coarsening. From this logarithmic plot, it is clear that the measured $P_N(V)$ does not follow a simple power law form. The observation that there are many grains with small volumes is reasonable since, during coarsening, there are always grains that are tending to zero volume as they are being consumed by larger grains.

Fig. 3b is a simple histogram of reduced spherical equivalent radii. Note, however, that volume is the measured physical quantity and the grains are far from being spherical; the radius, while being easily computed from the volume measurement and convenient for some purposes (see below), is not a physical characteristic of the grains. Nevertheless, Fig. 3b shows an apparent peak around $R/\langle R \rangle \sim 0.4$ which is qualitatively consistent with other data sets, see, for example, [23, 25, 38, 39] Figs. 3a and b are consistent with each other since the probability density functions for radius, P_r, and volume, P_V, are related by $P_r(r) = 4\pi r^2 \, P_V(V(r))$. The factor of $4\pi r^2$ is present due to the fact that the volume interval covered by dr scales with the surface area of the sphere.

At least two biases could be present in the size distributions shown in Fig. 3. The maximum grain size included is $\approx 5 \times 10^5 \ \mu m^3$ which corresponds to a spherical equivalent diameter (SED) of 100 μm which is comparable to the vertical size of the measured volume ($H_e = 195 \ \mu$m). The center of such a spherical grain would have to be well centered in the measured volume in order to not be eliminated from the statistics used here. A rough correc-
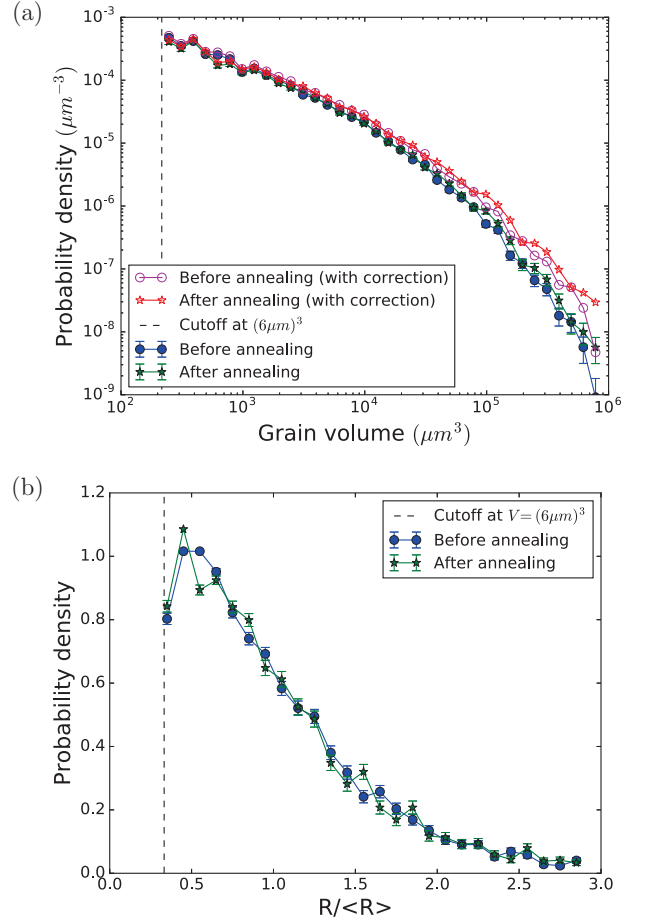

FIG. 3. Estimated grain volume probability densities, $P(V)$, with units of μm^{-3}, in each of the two measured states. Closed symbols are directly computed from the data while open symbols are corrected by (3). b) The reduced radius distributions corresponding to (a) without the finite volume correction. See the text for discussion.

tion that accounts for the reduction in volume available for the center of mass of a spherical grain of diameter D is

$$P_\infty(V)dV \approx \frac{dN}{N} \frac{1}{(1 - \frac{D}{L_e})^2 \, (1 - \frac{D}{H_e})}, \qquad (3)$$

where $D = 2 \left(\frac{3}{4\pi} V \right)^{1/3}$ and L_e is the measured square cross section side length and H_e is the height of the measured volume. Open symbols in Fig. 3 show these corrected values for the post-annealing state. As seen in Fig. 2, typical measured grains are not particularly spherical and this may increase or decrease the appropriate correction factor depending on anisotropy relative to the shape of the anisotropic measured volume.

The second possible bias in Fig. 3 occurs at small grain sizes where diffraction signals may become weak and lead to reduced sensitivity. The cutoff in grain size described in Sec. II B helps to assure that this effect is not present

or not large in the distributions shown. In fact, using a less aggressive cutoff shows a continued increase in the number of observed grains below the volume limit in Fig. 3a.

Over most of the volume range, the shape of Fig. 3a is essentially unchanged while in the large grain limit a subtle (on the logarithmic scale) increase is seen which corresponds to the increased average grain volume. The finite volume correction tends to make the logarithmic plots more power-law like, but there remains significant curvature over the entire three and a half decades of volume variation. Without additional anneal states, it is not possible to speculate on a trend toward a power law behavior.
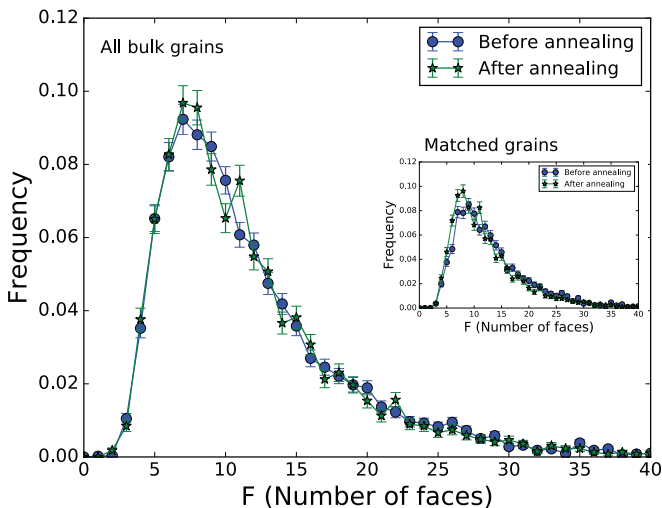
FIG. 4. The distribution of the number of faces or nearest-neighbors per grain in each measured state. The frequency is the number of occurrences of F, N_F, divided by the total number in each state. Error bars are $\sqrt{N_F}/N_{tot}$. There exist (but are not shown) grains that have values as high as $F = 80$. The inset shows the corresponding distribution for the 3299 matched grains whose evolution is discussed in Sec. III B.

b. *Number of faces distribution* The number of faces or nearest neighbors, F, of a grain is a fundamental topological quantity. [5, 6, 40] The distribution of F over the measured grains is shown in Fig. 4. Note that the inclusion of the large number of small, unresolved grains would increase the frequency of small neighbor numbers if they could be reliably included and a similar effect may reduce the large F limit of the distribution due to the finite measurement volume. For the included grains, the average number of faces is $\langle F_0 \rangle \approx 12.0$ in the initial state, and $\langle F_1 \rangle \approx 11.8$ in final state; the peak is at $F \approx 7.5$ in both states. This distribution, like the volume distribution, is essentially unchanged under the annealing. There is a long tail containing a small number of grains having as many as 80 neighbors (not shown). Not surprisingly, the grains in the tail of this distribution are also in the large grain tail of the volume distribution. The shape of the distribution shown here is similar to those seen in

Fig. 4b of Zhang et al. [23]; counting statistics do not allow detailed comparisons to their evolving distributions. Additional statistics are presented in the appendices.

B. Statistical characterization of grain evolution

Changes in grain size are expected to correlate with topological characteristics of grains and their neighborhoods. While the average behaviors shown below appear consistent with the isotropic theory, the variations within each topological class are found to be at least comparable to the overall variation in the average behavior.

a. *Dependence on number of grain faces* As a first statistic, consider changes in the spherical equivalent diameters of grains as a function of the grains' number of nearest neighbors. The spherical equivalent diameter is $D = 2 \left(\frac{3}{4\pi} V_g \right)^{1/3}$ and we use subscripts, 0 and 1 for the initial and annealed states. Note that most grains are far from spherical but D can be used as a linear characterization of size, growth, or shrinkage.
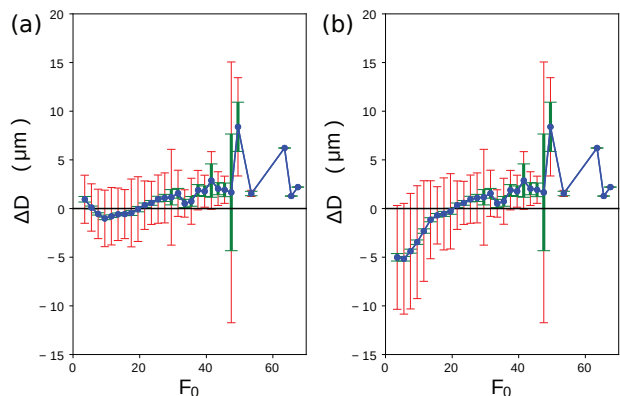

FIG. 5. Statistics of diameter changes for grains with different numbers of nearest neighbors (or faces) in the initial state. Pairs of face numbers have been binned for clarity. The mean (blue points) and standard deviations of the distributions in each bin (red vertical bars) are shown for each grain class. The smaller green error bars are the standard deviations of the estimated mean values, which are $\frac{1}{\sqrt{n}}$ times the distribution standard deviations (red error bars), where n is the number of grains in each bin. (a) includes only matched grains whereas (b) also includes a statistically estimated correction for grains that disappear and therefore have $\Delta D = -D_0$ (see text for discussion).

Fig. 5(a) shows diameter differences, $\Delta D = D_1 - D_0$, for each of the 3299 matched grains as a function of F_0, the number of faces in the initial state. Since F_0 correlates with grain size and large grains are expected to grow, a positive correlation of ΔD with F_0 is expected. The appropriate trx end in the mean is apparent in the figure, apart from the upturn at small face numbers (see

below). However, for grains in each class, the standard deviation of diameter changes is comparable to the overall variation in the mean. The large standard deviations at $F_0 = 46$ and 48 and the lack of standard deviations at larger numbers are due to the fact that only one or a few grains exist at these face numbers. It is apparent that at each value of F_0, some grains grow while others shrink. In spite of the fact that large F_0 correlates with large grains, this metric alone is not predictive of even the binary question of growth versus shrinkage of a particular grain.

The upturn in ΔD at small F_0 may be counter intuitive, but can be attributed to the fact that only grains that survive the annealing are included. Many small grains (typically with small F_0) should contribute $\Delta D = -D_0$. This bias can be removed in a statistical way. As stated above, there are 30.2% of initial state grains that are not paired in the forward matching and 12.4% in backward matching. Again assuming no nucleation, 12.4% is the estimated error rate in matching and the remaining 17.8% (885 grains) should be roughly the number of grains that disappeared. We randomly choose 885 of the forward matching unpaired grains and assume that they had $\Delta D = -D_0$. Including these yields Fig. 5(b) with intuitively reasonable average behavior of shrinking grains with small F_0 and growing grains at large F_0.

The mean growth curves in Fig. 5 cross zero at $F_0^{stagnent} \approx 19$, larger than $\langle F \rangle \approx 12$. Fig. 4 shows that about 80% of grains have $F < F_0^{stagnent}$; nevertheless, only roughly 50 % of grains shrank and 50% grew. A recent isotropic phase-field simulation [39] yields both a zero average growth rate and an average face number of ≈ 15 for a variety of initial grain sizes and face number distributions and at different time points. These distinctions are discussed in Sec. IV.

b. Dependence on grain neighborhoods Under the assumption that grain boundary interface energies and mobilities are independent of the five crystallographic parameters specifying grain boundary character, grain growth process should be described by the MacPherson-Srolovitz model. [4] Mullins and von Neumann [5, 6] showed that the evolution of grain boundary interfaces is driven by the local mean curvature of that boundary, and as a result, the total volume growth rate is given by

$$\frac{dV}{dt} = V^{1/3}M\gamma g \tag{4}$$

$$g = -\frac{1}{V^{1/3}} \int_{\text{Faces}} \left(\frac{1}{R_1} + \frac{1}{R_2} \right) dS \tag{5}$$

where M is a mobility constant for the grain boundary, γ is the excess interfacial energy per unit area and g represents the normalized integral mean curvature of the grain faces. R_1 and R_2 are local radii of curvature of the boundary and dS is an element of interfacial area. It is based on (4) and (5) that MacPherson and Srolovitz were able to obtain (2).
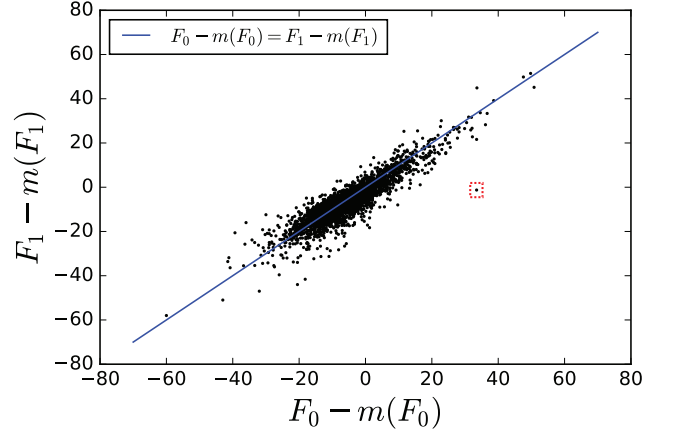

FIG. 6. Changes of the excess grain face number. Each point represents an individual grain. See discussion in the text. The outlier in the red box is discussed below in Sec. III C

To compare with our experimental data, Eq. (4) is converted to integral form, $\Delta V^{2/3} = \frac{2}{3} \int M\gamma g \, dt$. Earlier work by Rowenhorst et al. [38, 41] showed empirically that g is, at least in an averaged sense, proportional to $F - m(F)$, where F is the number of faces of a grain and $m(F)$ is the average number of faces of that grain's nearest neighbors; we refer to $F - m(F)$ as the "excess face number." As shown in Fig. 6, for most of the grains, the value of $F - m(F)$ does not change dramatically during the annealing. For grains with a given value in one state, the mean value in the other state is the same within a standard deviation of ≈ 4 . We infer that there should be a roughly linear relation between g and $F - m(F)$ and therefore that

$$\Delta V^{2/3} = V_1^{2/3} - V_0^{2/3} \propto \int [F - m(F)] \, dt \approx (F_1 - m(F_1)) \, \Delta t. \tag{6}$$
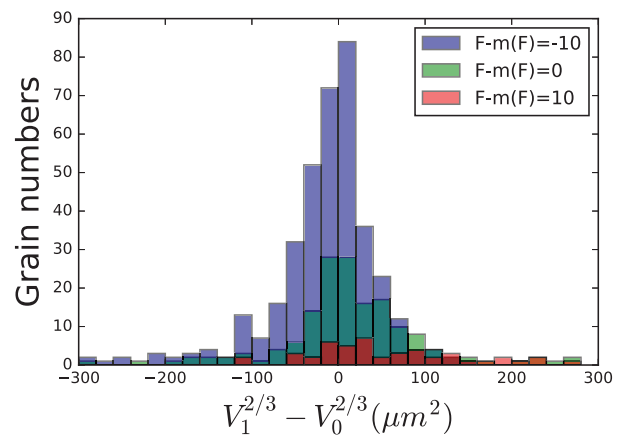

FIG. 7. Histograms of $\Delta V^{2/3}$ in (6) for three excess face numbers, $F - m(F)$. Here, $F = F_1$ is taken from the annealed state.

Fig. 7 demonstrates that the isotropic prediction Eq. (6) is not obeyed since for given values of $F - m(F)$, a wide distribution of values of $\Delta V^{2/3}$ is observed. On the other hand, there is a subtle shift of the histograms toward positive $\Delta V^{2/3}$ as the excess face number increases. It is also clear from these histograms that the total number of grains (integral under the curves) decreases strongly with increasing excess face number.

Fig. 8 shows the means and standard deviations of distributions like those shown in Fig. 7 over a broad range of excess face number. The range $-20 \le F_1 - m(F_1) \le 20$ corresponds a range over which the number of entries is large enough that the statistical result is robust. Remarkably, the mean values of the broad distributions do appear to roughly correlate with Eq. (6). The mean values roughly follow a straight line which crosses zero volume change near $F_1 - m(F_1) = 0$. However, the region $F_1 - m(F_1) < 0$, where neighbors have more faces than the grain in question, appears to deviate from the linear trend. As discussed with respect to Fig. 5, this is likely due to neglect of disappearing grains. Performing the same correction as in that case yields Fig. 8(b) with an improved linear region around zero volume change. The large standard deviations are consistent with Fig. 7 and are seen to be comparable to the overall trend in the mean.

Again in this case, the variation in response within each category, indicated by the standard deviation bars, is large and crosses zero volume change in almost every class. The average behavior is again not a good predictor of a particular grain's response. We discuss this failure, which is consistent with prior work [17, 23] in Sec. IV; the next section gives anecdotal examples of unexpected behaviors.
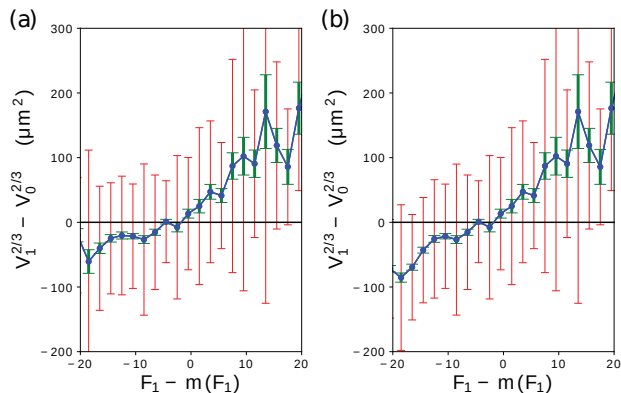

FIG. 8. Test of the linear relation of Eq. (6). (a) shows matched grains only while (b) includes a statistically estimated correction, based on the size distribution of unmatched grains, for grains that were consumed during annealing; these grains were assigned $V_1 = 0$. As in Fig. 5, blue points and red vertical bars are the means and standard deviations of the distributions in each bin (with examples shown in Fig. 7). The smaller green error bars are the standard deviations of the estimated mean values.

C. Examples of anomalous behavior

The large standard deviations discussed above imply that local fluctuations in behavior are important and that outlier behavior can be expected. While a comprehensive analysis of grain boundary movements correlated with grain boundary character is beyond the scope of this paper, we show here examples of counter intuitive behavior. These examples illustrate both intrinsic effects and ambiguities that arise from the parameters associated with defining and matching grains.
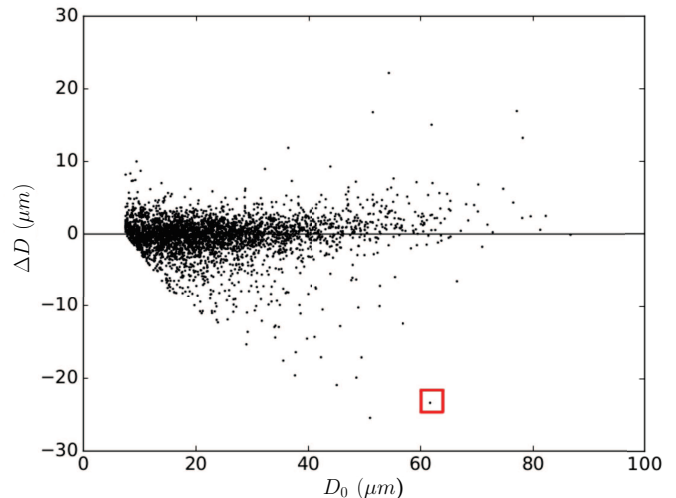

FIG. 9. Changes in diameter for all 3299 matched grains as a function of initial size. Each point represents a single grain. A large grain, discussed in Sec. III C that shrank during annealing is identified by red box.

Big vs. bigger In a large ensemble, it is not surprising to find two or more large grains that are nearest neighbors. Since "large" grains are expected to consume "small" ones, this is one mechanism to explain the observation that some large grains shrink. Such behavior is entirely consistent with curvature driven growth laws, either with or without the isotropy assumption. With the statistical correlation between face number and grain size shown in Fig. 14, this effect can explain at least some of the dispersion seen in Figs. 5 and 8.

Fig. 9 shows the change in spherical equivalent diameter for grains with a wide range of initial diameters. There is only a weak average trend for larger grains to grow, as is implicit in Fig. 5. Again, dispersion is the dominant feature. The red box indicates an initially large grain (initial SED of 62 μm or volume $\sim 10^5$ μm^3) that shrinks substantially during annealing. Fig. 10 shows this grain in yellow and two of its neighbors (green and purple) that are even larger in the two states. The yellow grain appears to be convex over much of the visible boundary and it is consumed by the large and oddly shaped green grain beneath it as well as by the unseen grain in front.
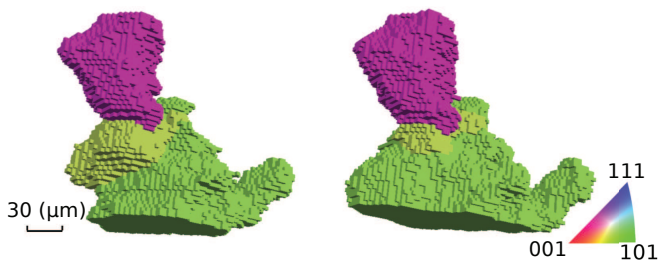
FIG. 10. The yellow grain is large but is seen to shrink during annealing. The bottom of the green grain is cut off by the end of the measurement volume.

a. Anomalous grain division and matching Another interesting case is the grain boxed in red in Fig. 6: in the initial state, it has a substantial excess number of faces, $F_0 - m(F_0) \approx 35$. But the grain boundary topology changed dramatically during annealing so that $F_1 - m(F_1) \approx 0$ afterwards. After some investigation, it turns out that the relevant grain (light blue) was split in two by a growing small grain, as shown in Fig. 11. The grain matching algorithm, when run in the forward direction, matched the initial grain to one of the two split grains, resulting in the dramatic reduction in excess face number. In the reverse direction, both split grains are matched to the same initial whole grain. This anomalous behavior also caused the unexpected drop in Fig. 5 between $40 < F_0 < 50$. The mystery, of course, is why did the small yellow grain succeed in growing through its larger neighbor? An alternate explanation would be some sort of unexpected reconstruction artifact in one or the other state.
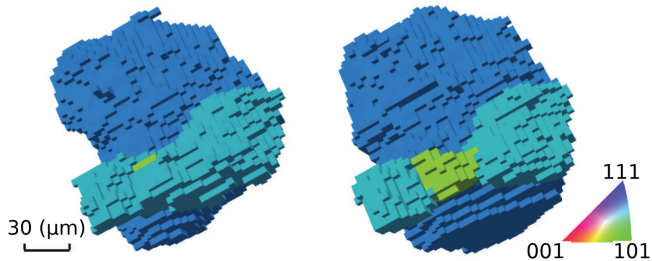

FIG. 11. The light blue grain in the initial state (left) is split in two (right) by a growing small yellow grain. The flat bottom of the large dark blue grain in the annealed state indicates that it reached the edge of the measurement volume.

b. Apparent grain rotation For grains with diameters of several microns and larger, grain rotation is not expected during the coarsening process because the constituent crystallites are highly constrained by their neighbors. The distribution of disorientation angles between matched grain pairs are shown in Fig. 16c. Most have $\leq 0.1°$ disorientations which is the resolution of the measurement and is therefore consistent with zero. However, there are several cases (out of 3299 matched pairs) where

the disorientations are $> 0.2°$. Fig. 12 explains one extreme case and shows that this case is an artifact of the arbitrary threshold used in segmenting grains. The two grains shown are separated by a low angle boundary, indicated by the black lines, of $\approx 1.8°$ disorientation. With the disorientation tolerance of $2°$ used in *DREAM.3D* for segmenting voxels into grains, these two grains were grouped together as one. The change of relative volumes caused by motion of the low angle boundary during annealing caused the grain average orientation to change while the orientations of each sub-grain did not change beyond the experimental resolution. Again, the grain matching algorithm in this paper uses the disorientation angle as one of its criteria, so it may miss grain pairs whose average orientation rotated too much ($> 0.5°$) due to such low angle boundary motions.
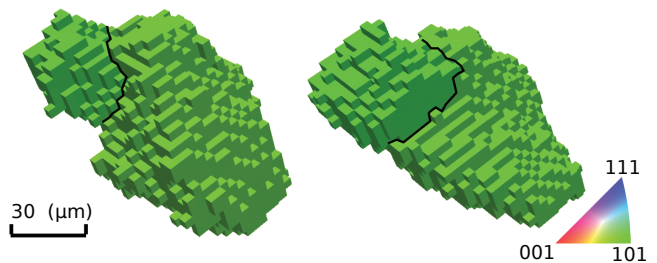

FIG. 12. Two grains that have a low angle boundary of $\approx 1.8°$ disorientation, indicated by the black lines. With the disorientation tolerance ($= 2°$) used in *DREAM.3D*, they were considered together as one grain, so the change of relative volume ratio caused the change of the average grain orientation.

IV. DISCUSSION

Near-field high energy x-ray diffraction microscopy makes possible this statistical study of α phase iron grain coarsening. Over 10,000 grains are reconstructed with the forward modeling method [19, 29] in each of two sample states. The grain statistics and changes thereof presented here are not dependent on resolution of individual grain boundaries and therefore do not involve boundary smoothing and tracking. On the other hand, the estimation of the probability density for finding grains of volume V (Fig. 3) is affected by the finite measured volume and finite experimental resolution. We give an estimated correction for the finite volume effect and we use a conservative small size cut-off to avoid distortions due to reduced sensitivity in this limit. The most significant contribution to uncertainty in the grain evolution analysis is the lack of perfect matching of grains between the two states; this problem is most apparent for small grains as shown in Appendix B but also has a contribution due to initial grains that grow past the boundaries of the measured volume in the final state.

We assume that new grains do not nucleate in the

fully recrystallized material with tens of micron grain dimensions. While rare exceptions have been observed in nickel [42] associated with very low energy annealing twin formation, corresponding low energy boundaries are not available in the α phase, bcc structure measured here. The lack of large twin populations simplifies analysis relative to current studies of nickel. [43]

In an averaged sense, the isotropic model for coarsening that assumes that all boundaries have the same energy and mobility compares very well with the observed grain evolution. This implies that the normalized mean curvature alone can be used to describe average grain growth behavior. However, as shown in Figs. 5 and 8, individual grains within a topological class vary in their growth by as much as $\sim \pm 100\%$ of the observed range of average behaviors. This range of variation is consistent with prior observations of coarsening in two dimensional succinonitrile $(C_2H_4(CN)_2)$ polycrystals [17], with recent observations of iron by Zhang et al., [23] and with our observations of nickel. [43] In the succinonitrile case, the authors observed that the growth rate of the average grain area, $\langle A \rangle$, within topological classes specified by the number of grain sides or neighbors, n, was consistent with the classic, isotropic $n - 6$ dependence. [5, 6] But, similar to the recent observations, large variations from grain to grain were observed with variations in each class of order 100% of the observed range of averaged behaviors.

There are a number of possible origins of the observed large dispersion in growth characteristics within topological classes. i) The empirical relation between $F - m(F)$ and mean curvature, g, itself has substantial dispersion but less than the range of variation in g. [38] It is based on experimentally measured curvatures so a portion of observed dispersion may be due to measurement uncertainties. It appears that this contribution does not account for observed variations in Figs. 7 and 8. ii) During the annealing used here, the values of $F - m(F)$ are not constant as shown in Fig. 6. However, given the slope of the mean in Fig. 8, changes of ± 4 as consistent with Fig. 6 are not sufficient to generate the observed large distribution widths. iii) More interestingly, grain boundary energies and mobilities are, in fact, not uniform and the inclusion of many boundary types within topological classes can be expected to generate dispersion in the statistics presented here. Further, Zhang et al. [23] speculate that their observed reduction in growth rate may be associated with large variations in mobility. These observations strongly motivate on-going work that will analyze motions of individual boundaries and that can extract, for example, boundary energy distributions. [44] Further experimental work is certainly warranted. Extending measured volumes while maintaining comparable grain sizes can increase the dynamic range of the measurements. Expanding the range of growth may elucidate how distributions evolve toward the steady state.

On a measurement technique note, the apparent near-field HEDM measurement sensitivity to almost four decades in grain volume while the detector sensitivity spans only about three decades can be understood from the fact that observed intensities on the near-field detector do not scale with grain volume as they do in a more traditional (or in a far-field HEDM [28]) measurement. In a sub-grain resolved diffraction measurement, detector pixel intensities are proportional to the sub-volume of the grain, $V_{(j,k)}^{grain}$, that projects intensity to the pixel rather than the entire grain volume. Here, (j, k) specifies a pixel coordinate. For a large grain, $V_{(j,k)}^{grain}$ is proportional to the pixel area (and the beam height and geometric factors specifying the scattering geometry for a given Bragg peak). Until the volume "seen" by the pixel starts to extend beyond the grain's boundaries (due to either small grain size or when scattering originates from near a boundary of a large grain) the intensity is independent of grain size.

V. CONCLUSIONS AND PROSPECTS

New x-ray probes of three dimensional grain geometries and evolution which study significant volumes of microstructure are leading to improvements in understanding of grain coarsening phenomena. The summary statement at this point is that averages over topological classes follow expected behavior based on isotropic models of curvature driven evolution, but that individual grains deviate by large amounts from this simplified model.

Further understanding can be expected based on the combination of improved experimental methods and facilities and on the use of modern numerical methods. For example, it appears to now be practical to extract grain boundary energies from geometries of very large numbers of triple junctions [44] such as measured here. This approach may then provide a means for separating the roles of energy and mobility. It has also been suggested that this separation may be possible through purely experimental observations of boundary motions. [30]

Appendix A: Statistical distributions

Fig. 13 shows the distributions of disorientations at grain boundaries, weighted by boundary area (the boundary area is calculated without any smoothing, so this is larger than the real boundary area). Note that the distributions are similar to the Mackenzie distribution, but are slightly larger than random for low angle boundaries and there is a deficit near the peak at 45°. These features, as well as the peak at 60°, reflect the anisotropic grain boundary energies presented in Ref. [45]. As expected, the peak due to the low energy twin boundaries at 60° is weaker than that found in fcc nickel. [27]
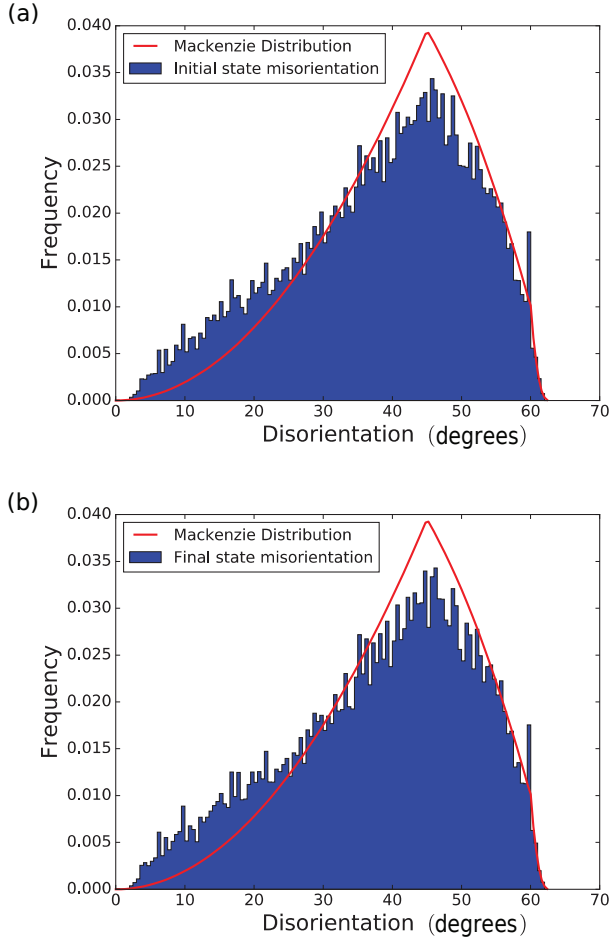

FIG. 13. Disorientation distribution with bin size equal to 0.5°. The solid red line is the Mackenzie distribution [46] for randomly oriented cubes. The distribution is essentially unchanged during annealing.

Other important statistics are about grain faces. Fig. 14 confirms that on average larger grains have more faces than small grains. The dispersion in the SED values here is smaller than the overall trend, in contrast to the growth characteristics discussed in the text.
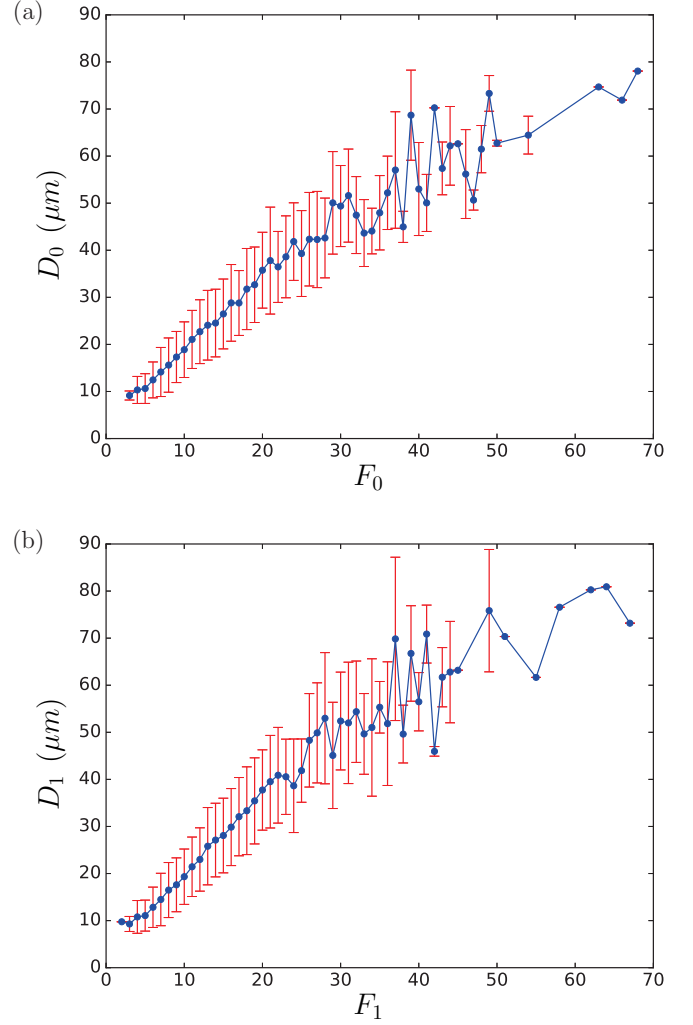
Fig. 15, similar to Fig. 7 of [38], shows that grains

FIG. 14. Relation between grain spherical equivalent diameter and the number of nearest neighbors, F. The grains with the same numbers of neighbors are grouped together and the mean (blue line) and standard deviation (red bar) are calculated for each group. (a) initial state, (b) final state.

with small face numbers, F, are likely to be surrounded by grains having more faces; grains with $F \approx 18$ have zero excess face number, which is consistent with Figs. 5 and 8. Fig. 8 shows that this value separates, on average, grains that grow from grains that shrink. However, this criterion is not predictive for individual grains. These plots are similar to, but with slightly different parameters from plots seen in, for example, Refs. [38, 39].

Appendix B: Matched grain pair characteristics

The following figures show statistical analysis of the grain pairs found through the analysis described in Sec. II C. These figures validate the parameters used in the grain matching algorithm. Fig. 16a shows the size ratios
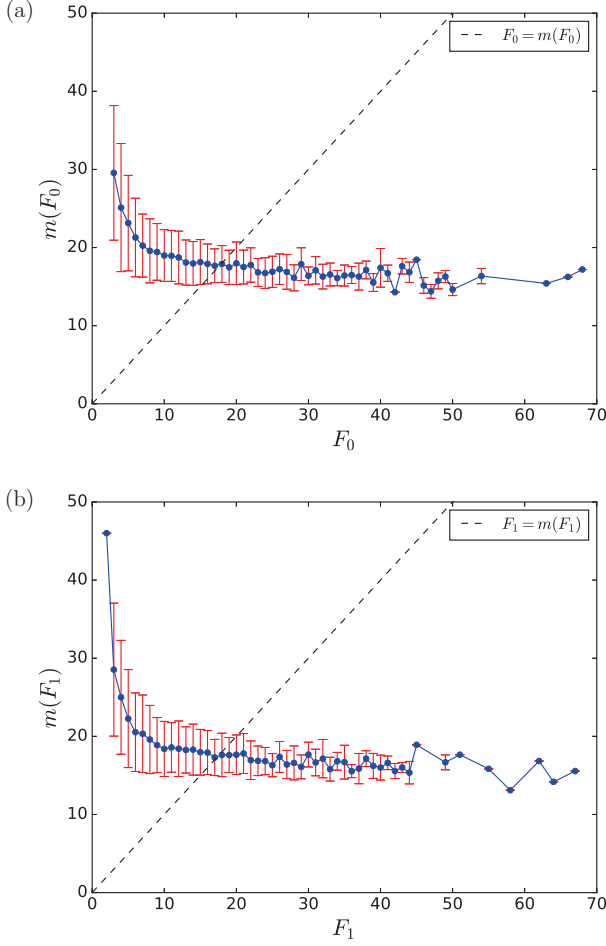
FIG. 15. Aboav-Weaire plots [47, 48] giving the relation between the number of neighbors a grain has, F, and the average number of neighbors its neighbors have, $m(F)$. Subscripts on F indicate (a) initial and (b) final anneal states. Grains with each neighbor number F are grouped together and the mean (blue) and standard deviation (red) of $m(F)$ for those grains are plotted. The dashed line separates regions in which $m(F) > F$ (upper left) from the region with $m(F) < F$ (lower right).

of paired grains. Of the tracked grains, roughly as many decreased in size as increased. Of course, many grains disappeared or were consumed by others (and therefore were not matched); such events break the near-symmetry and result in increased average grain size.

Fig. 16b shows the ratio of center-of-mass displacements to the spherical equivalent diameter in the final state. Most displacements are less than one diameter but a few are substantially larger indicating asymmetric growth, which results primarily from some small grains.

The misorientation angles between tracked grains in the initial state and after annealing are shown in Fig. 16c to be generally less than 0.1° which is the nominal resolution of the measurement. A small number of pairs extend up to the maximum rotation allowed by the pa-

rameters used in the matching algorithm. The cut-off at $\approx 0.04°$ probably indicates residual misalignment of the two sample states.

Figs. 16d - 16f show individual center-of-mass displacement components in the sample coordinate system. The mean values correspond to $\approx (-7, 10, 4)$ μm with x and y being in the plane of each layer measurement and z being perpendicular thereto. With average grain diameters of ≈ 30 μm, these displacements are consistent with data of Fig. 16b. The fact that these component displacements are not centered on zero may indicate a residual lack of alignment or simply the statistics of grains that were tracked. Note that the average z-displacement corresponds to roughly one layer spacing in the measurement; the in-plane voxel side lengths are 3 μm.

Next, we turn to the statistics associated with unmatched grains. Fig. 17a shows the size distribution of unmatched grains in each state. Most contain fewer than 100 voxels in the initial state and an even tighter distribution in the final state. Many of these grains may have been consumed during annealing and therefore are not present after annealing. However, those grains having spherical equivalent diameters < 5 μm, which is less than the offsets shown in Figs. 16d - 16f, also may have been rejected by the matching algorithm. In addition, smaller grains may tend to have larger volume change ratios, which is another reason that they could be wrongly rejected by the matching algorithm. Fig. 17b shows the vertical position distribution of unmatched grains, which is roughly uniform as expected. There are slightly more unmatched grains at the bottom edge of the initial state and the top edge of final state; this is consistent with Fig. 16f which shows a ~ 4 μm offset between the two volume measurements.
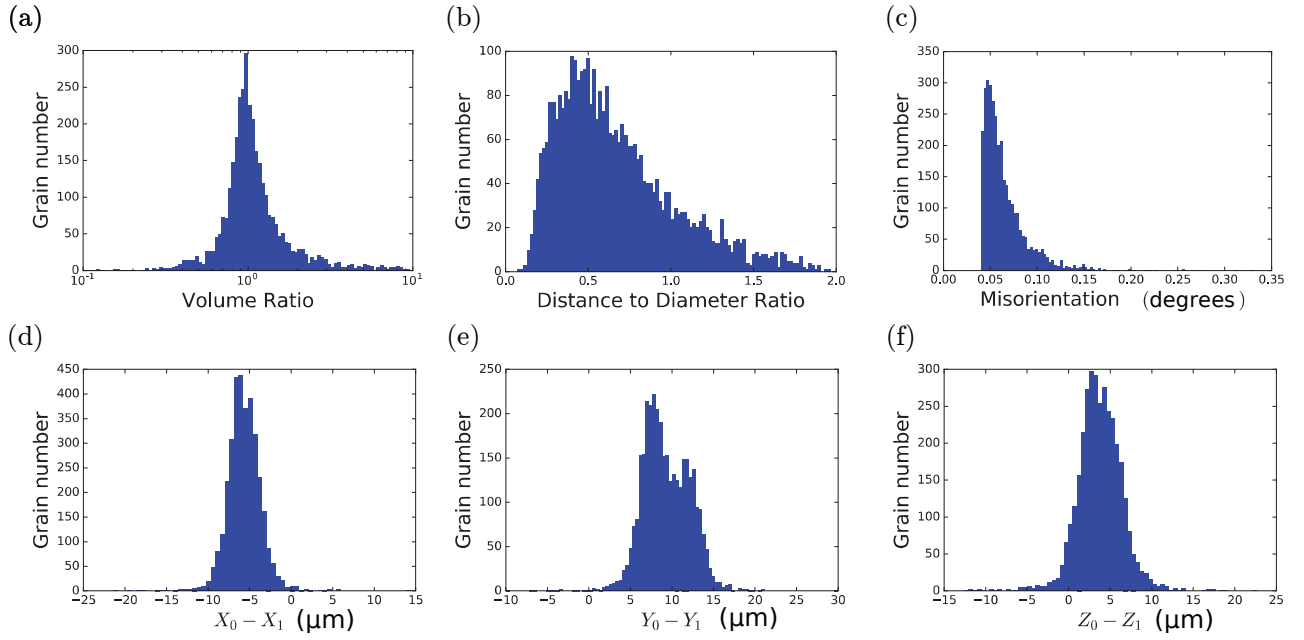
FIG. 16. Distributions of matched grain properties. (a) shows the ratio of spherical equivalent diameters, D_1/D_0; (b) shows the distance between centers-of-mass in the two states divided by D_0; (c) demonstrates that the rotation angle required to bring matched grain orientations in the two states into coincidence is typically less than 0.1 degree; (d) through (f) show the center-of-mass displacements between states in Cartesian component form; the z direction is perpendicular to the line focused x-ray beam plane.
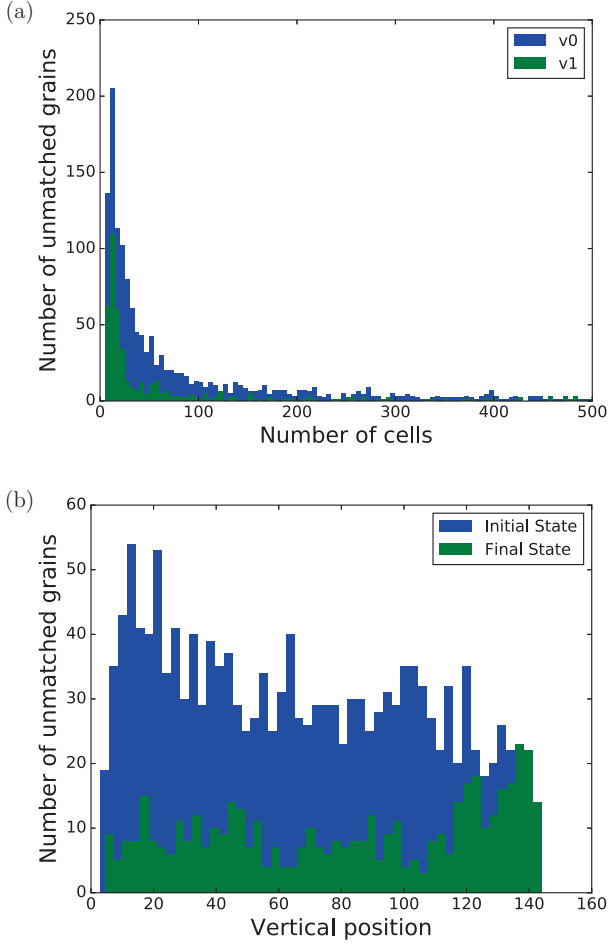
FIG. 17. Statistics of unmatched grains. (a) Shows the size distributions in each state in terms of the number of $3 \times 3 \times 3$ μm^3 cells, each of which corresponds to about eight reconstructed voxels. A small number of larger unmatched grains are not shown. (b) Shows the locations in z coordinate in microns of unmatched grains.

[1] J.Wang, A. Nguyen, and S. Farrokhpay, Advances in Colloid and Interface Science **228**, 55 (2016).

[2] S. Hilgenfeldt, S.A. Koehler, and H.A. Stone, Phys. Rev. Lett. **86**, 4704 (2001).

[3] S. Magrabi, B. Dlugogorski, and G. Jameson, Chemical Engineering Science **54**, 4004 (1999).

[4] R. D. MacPherson and D. J. Srolovitz, Nature **446**, 1053 (2007).

[5] J. Von Neumann, Ohio: American Society for Metals , 108 (1952).

[6] W. W. Mullins, Journal of Applied Physics **27**, 900 (1956).

[7] G. S. Rohrer, Journal of Materials Science **46**, 5881 (2011).

[8] E. O. Hall, Proceedings of the Physical Society. Section B **64**, 747 (1951).

[9] N. Petch, Journal of the Iron and Steel Institute **174**, 25 (1953).

[10] K. S. Chan, International Journal of Fatigue **32**, 1428 (2010).

[11] C. S. Smith, Metal Interfaces , 65 (1952).

[12] C. S. Smith, Metallurgical Reviews **9**, 1 (1964).

[13] M. Selleck, K. Rajan, and M. Glicksman, Simulation and Theory of Evolving Microstructures , 79 (1989).

[14] M. Anderson and A. Rollett, Metals and Materials Society, TMS Publication (1990).

[15] G. Abbruzzese, I. Heckelmann, and K. Lücke, Acta Metallurgica et Materialia **40**, 519 (1992).

[16] G. Gottstein, A. Rollett, and L. Shvindlerman, Scripta Materialia **51**, 611 (2004).

[17] M. Palmer, V. Fradkov, M. Glicksman, and K. Rajan, Scripta Metallurgica et Materialia **30**, 633 (1994).

[18] E. M. Lauridsen, S. Schmidt, R. Suter, and H. F. Poulsen, Journal of Applied Crystallography **34**, 744 (2001).

[19] R. Suter, D. Hennessy, C. Xiao, and U. Lienert, Review of Scientific Instruments **77**, 123905 (2006).

[20] H. Poulsen, *Three-Dimensional X-ray Diffraction Microscopy*, edited by G. Hohler, Vol. 205 (Springer Tracts in Modern Physics, Berlin, 2004).

[21] W. Ludwig, S. Schmidt, E. Lauridsen, and H. Poulsen, J. Appl. Cryst. **41**, 302 (2008).

[22] W. Yang, B. Larson, J. Tischler, G. Ice, J. Budai, and W. Liu, Micron **35**, 431 (2004).

[23] J. Zhang, Y. Zhang, W. Ludwig, D. Rowenhorst, P. Voorhees, and H. Poulsen, Acta Materialia **156**, 76 (2018).

[24] I. McKenna, S. Poulsen, E. Lauridsen, W. Ludwig, and P. Voorhees, Acta Materialia **78**, 125 (2014).

[25] J. Sun, A. Lyckegaard, Y. Zhang, S. Catherine, B. Patterson, F. Bachmann, N. Gueninchault, H. Bale, C. Holzner, E. Lauridsen, and D. J. Jensen, in *IOP Conf. Ser: Mater. Sci. Eng*, Vol. 219, 2017 (2017).

[26] S. McDonald, P. Reischig, C. Holzner, E. M. Lauridsen, P. Withers, A. Merkle, and M. Feser, Scientific Reports **5**, 14665.1 (2015).

[27] C. Hefferan, S. Li, J. Lind, and R. Suter, Advances in X-ray Analysis **53** (2009), 10.1154/1.3427328.

[28] U. Lienert, S. Li, C. Hefferan, J. Lind, R. Suter, J. Bernier, N. Barton, M. Brandes, M. Mills, M. Miller, B. Jakobsen, and W. Pantleon, JOM **63**, 70 (2011).

[29] S. Li and R. Suter, Journal of Applied Crystallography **46**, 512 (2013).

[30] S. Maddali, *Computational mining of meso-scale physics from high-energy X-ray data sets*, Ph.D. thesis, Carnegie Mellon University (2016).

[31] S. Li, *Imaging of Orientation and Geometry in Microstructures: Development and Applications of High Energy X-ray Diffraction Microscopy*, Ph.D. thesis, Carnegie Mellon University (2011).

[32] C. M. Hefferan, *Measurement of Annealing Phenomena in High Purity Metals with Near-field High Energy X-ray Diffraction Microscopy*, Ph.D. thesis, Carnegie Mellon Univeristy (2012).

[33] M. Syha, *Microstructure Evolution in Strontium Titanate*, Ph.D. thesis, Karlsruher Institut fr Technologie (KIT) (2014).

[34] S. Schmidt, S. Nielsen, C. Gundlach, L. Margulies, X. Huang, and D. J. Jensen, Science **305**, 229 (2004).

[35] J. Lind, A. Rollett, R. Pokharel, C. Hefferan, S. Li, and R. S. U. Lienert, in *IEEE International Conference on Image Processing (ICIP)*, IEEE International Conference Image Processing (2014) pp. 4877–4881.

[36] D. Menasche, P. Shade, and R. Suter, "Accuracy and precision of near-field hedm forward model based microstructure reconstructions," (unpublished).

[37] M. A. Groeber and M. A. Jackson, Integrating Materials and Manufacturing Innovation **3**, 5 (2014).

[38] D. Rowenhorst, A. Lewis, and G. Spanos, Acta Materialia **58**, 5511 (2010).

[39] V. Yadav and N. Moelans, Acta Materialia **156**, 275 (2018).

[40] W. Mullins, Journal of Applied Physics **59**, 1341 (1986).

[41] X. Zhong, D. J. Rowenhorst, H. Beladi, and G. S. Rohrer, Acta Materialia **123**, 136 (2017).

[42] B. Lin, Y. Jin, C. Hefferan, S. Li, J. Lind, R. Suter, M. Bernacki, N. Bozzolo, and G. R. A.D. Rollet and, Acta Materialia **99**, 63 (2015).

[43] A. Battacharya, Y. Shen, C. Hefferan, S. Li, J. Lind, R. Suter, and G. Rohrer, Acta Materialia **167**, 40 (2019).

[44] Y. Shen, X. Zhong, H. Liu, R. Suter, A. Morawiec, and G. Rohrer, Acta Materialia **166**, 126 (2019).

[45] S. Ratanaphan, D. Olmsted, V. Bulatov, E. Holm, A. Rollett, and G. Rohrer, Acta Materialia **88**, 346 (2015).

[46] J. K. Mackenzie, Biometrika **45**, 229 (1958).

[47] D. A. Aboav, Metallography **3**, 383 (1970).

[48] D. Weaire, Metallography **7**, 157 (1974).